Journal of Sound and Vibration (2000) **235**(5), 763–786
doi:10.1006/jsvi.2000.2977, available online at http://www.idealibrary.com on IDEAL®

VIBRATIONS OF A FOUR-DEGREE-OF-FREEDOM RIGID BODY SLIDING AGAINST A WAVY SURFACE

C. Pholsiri and M. D. Bryant

Department of Mechanical Engineering, The University of Texas at Austin, Austin, TX 78712-1063, *U.S.A. E-mail: longrath@mail.utexas.edu; mbryant@mail.utexas.edu*

(*Received* 22 *October* 1998, *and in final form* 1 *February* 2000)

It has been shown that certain patterns of surface waviness on a counter surface, in conjunction with speed and stiffness of a slider can create vibrations that reduce slider wear. This study attempts to simulate these vibrations, with the goal of understanding how the slider interacts with the surface waviness, to produce a given vibration. This paper develops a model of a four-degree-of-freedom rigid body pressed against a sliding counter surface, and studies its vibration motions under several conditions. The four degrees of freedom include one translation normal to the sliding surface and three rotations. The effects of waviness of the counter surface on the system responses are also studied. To model loading effects between the slider and a wavy counter surface that has multiple points of contact, an equivalent contact point is defined that is assumed to move along a certain path on the slider's contact surface. Several possible paths of the equivalent contact point over the slider face were studied, and their effects are discussed. With appropriate choice of parameters, the simulation results were comparable to experimental results obtained in a previous study.

1. INTRODUCTION

It has long been known that vibrations can reduce friction [1–5]. Vibrations can also reduce sliding wear. Bryant *et al.* [6, 7] and Tewari [8] found that wear particles detached from brushes sliding against smooth rotors were larger than those detached sliding against wavy rotors. Finding wear rates lower when sliding on wavy rotors than on smooth rotors, Bryant co-workers [9–11] suggested that waviness of the mating surface could significantly reduce brush wear rates without contact separations. The authors claimed that wear reduction was due to micro-vibrations induced by the surface waviness. Contact voltage drop tests [7] indicated that the wear reduction was not due to separation of surfaces.

Conducting experiments in which wear rates of carbon brushes at different clearances between brush and brush holder were compared, York [12] and Bryant *et al.* [7] reported that a proper amount of clearance could reduce wear rates up to 50%. The optimal amount of clearance was correlated to the wear particle size. The author hypothesized that, with a proper amount of clearance, the brush could rock within its holder. This created a gap through which wear particles could escape without scratching the brush's bottom surface. However, when the clearances were too large, the brush banged against the inner sides of the holder, increasing wear.

More recent experiments by Bryant and York [13] slid a carbon graphite block over a wavy steel counter surface. Using a capacitance gauge, they measured the resulting rigid-body vibration displacements induced by the surface waviness, and correlated these

0022-460X/00/350763 + 24 $35.00/0

vibratory motions to measurements of wear. They found a correlation between wear rate and kinetic energy of vibration. In reference [13], a sample, spring loaded in a holder, slid against a rotor that had a three-dimensional surface waviness topography. Surface waves from this topography passed beneath the slider and forced the slider to vibrate: translate normal to the sliding surface, and rock or rotate with rotation vectors parallel and perpendicular to the sliding direction. A micron resolution capacitance gauge measured translation motions along directions (X, Y, Z) shown in Figure 1; displacements X and Y were converted into rocking rotations θ and ϕ parallel and perpendicular to the sliding direction X. During these experiments, York [12, 7] found that rocking vibrations with rotation vector perpendicular to the direction of sliding generated acoustic noise, and often were associated with stick/slip at the leading or trailing edge of the slider. Conversely, rocking vibrations with rotation vector parallel to the direction of sliding were much quieter.

Swayze and Akay [14] developed a vibration model of a two-dimensional rigid-body sliding against a smooth surface. They studied stability of the system with respect to system parameters. This paper extends the Swayze and Akay work [14] to four degrees of freedom (d.o.f.), and uses this vibration model to simulate sliding against wavy counter surfaces. The goal is to understand friction and wear reduction phenomena caused by vibrations. Swayze and Akay's simulations featured rigid-body translations normal to the sliding surface, and rocking with a rotation vector perpendicular to the sliding direction. As mentioned earlier, York's experiments [12, 7] found that these vibrations generated substantial acoustic noise. More d.o.f are needed to simulate York's other rocking case, with rotation vector parallel to sliding, which seemed to suppress noise and slip/stick.

In this paper, a model for a four-d.o.f. rigid-body sliding against a smooth surface will be developed, the equations will be verified analytically and numerically, a stability analysis will be performed, and then a surface waviness excitation will be added with simulations thereof presented. These simulations will then be compared to measurements found in reference [13].

2. MODEL FORMULATION

Figure 1 shows the 3-D rigid body pressed against a counter surface moving with speed U in the positive X direction. Co-ordinate system (X, Y, Z) is an inertial frame; system (x, y, z) is attached to the center of mass of the rigid body. The slider can translate vertically (along $Z \leqslant 0$), but is constrained in the other directions (X and Y). The slider can rotate about all three axes. The rigid body has dimensions $(2h_x, 2h_y, 2h_z)$ along (x, y, z) respectively. A static vertical force, $F_{st} \geqslant 0$, is applied at the center of mass to promote contact between the slider and the counter surface. Rotations of the body about (x, y, z) are described by Euler's angles (ϕ, θ, ψ) [15].

2.1. EQUATIONS OF MOTION

Consider the case when $\phi, \theta > 0$. For a rectangular parallelepiped slider, the contact point is at the corner at the co-ordinate $(-h_x, h_y, h_z)$ in the xyz system. This results in an upward movement of the center of mass of the slider. The vertical displacement Z in the XYZ system due to small rotations ϕ and θ be determined by transforming the distance between the center of mass and the contact point in the xyz to the XYZ co-ordinates through the transformation matrix $[T]$ (equation (A5)) and then by subtracting that value

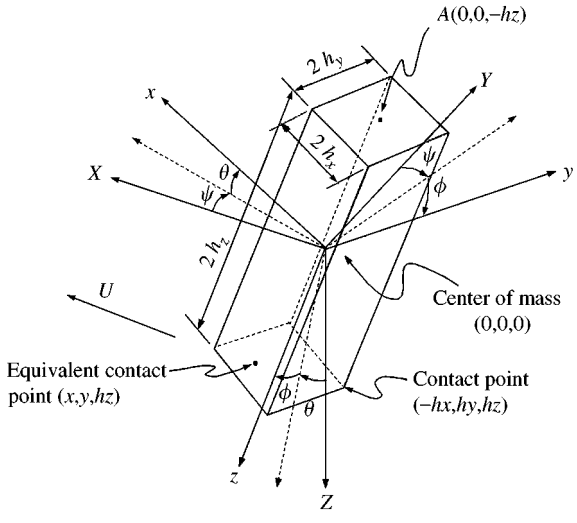

Figure 1. A slider of dimensions $2h_x \times 2h_y \times 2h_z$ pressed against a counter surface which moves with speed U in the X direction. Variables θ, ϕ, ψ measure angular displacements about y-, x-, and z-axis; Z measures vertical displacements. The XYZ co-ordinate system is fixed, xyz system is attached to the slider. The contact point when $\phi, \theta > 0$ is shown.

from the initial distance h_z:

$$Z = -[h_x \sin\theta + h_y \cos\theta \sin\phi - h_z(1 - \cos\theta\cos\phi)]. \tag{1}$$

Displacements Z of the center of mass in the Z direction are governed by

$$m\ddot{Z} = F_{st} - b_z\dot{Z} - k_z Z - F_n, \tag{2}$$

where m is the mass of the slider, b_z and k_z are damping and stiffness coefficients for motions along the Z-axis, and F_n is the total normal force in the Z direction that presses the slider against the counter surface. Substitution of equation (1) into equation (2) permits evaluation of

$$\begin{aligned} F_n = {} & F_{st} - k_z(h_z - h_z\cos\phi\cos\theta - h_y\cos\theta\sin\phi - h_x\sin\theta) \\ & - b_z(h_z\cos\phi\sin\theta\dot{\theta} + h_z\cos\theta\sin\phi\dot{\phi} - h_y\cos\phi\cos\theta\dot{\phi} - h_x\cos\theta\dot{\theta} \\ & + h_y\sin\phi\sin\theta\dot{\theta}) - m[(h_z\sin\phi\cos\theta - h_y\cos\phi\cos\theta)\ddot{\phi} + (h_z\cos\phi\sin\theta \\ & + h_y\sin\phi\sin\theta - h_x\cos\theta)\ddot{\theta} + (h_z\cos\phi\cos\theta + h_y\cos\theta\sin\phi)\dot{\phi}^2 \\ & + (h_x\sin\theta + h_y\cos\theta\sin\phi + h_z\cos\phi\cos\theta)\dot{\theta}^2 + 2(h_y\cos\phi\sin\theta \\ & - h_z\sin\phi\sin\theta)\dot{\phi}\dot{\theta}] \end{aligned} \tag{3}$$

Rotations (ϕ, θ, ψ) about the xyz axes are governed by Euler's equations [15]

$$M_x = I_{xx}\dot{\omega}'_x - (I_{yy} - I_{zz})\omega'_y\omega'_z, \quad M_y = I_{yy}\dot{\omega}'_y - (I_{zz} - I_{xx})\omega'_z\omega'_x, \tag{4a, b}$$

$$M_z = I_{zz}\dot{\omega}'_z - (I_{xx} - I_{yy})\omega'_x\omega'_y \tag{4c}$$

and from reference [15],

$$\omega'_x = \dot{\phi} - \dot{\psi}\sin\theta, \quad \omega'_y = \dot{\theta}\cos\phi + \dot{\psi}\cos\theta\sin\phi, \tag{5}$$
$$\omega'_z = \dot{\psi}\cos\theta\cos\phi - \dot{\theta}\sin\phi.$$

Substituting equations (5) into equations (4), we obtain

$$M_x = I_{xx}(\ddot{\phi} - \sin\theta\ddot{\psi} - \cos\theta\dot{\psi}\dot{\theta}) - (I_{yy} - I_{zz})(\cos\theta\sin\phi\dot{\psi} + \cos\phi\dot{\theta}) \times (\cos\phi\cos\theta\dot{\psi} - \sin\phi\dot{\theta}), \tag{6a}$$

$$\mathrm{M}_y = I_{yy}(\cos\phi\ddot{\theta} + \cos\theta\sin\phi\ddot{\psi} - \sin\phi\sin\theta\dot{\psi}\dot{\theta} + \cos\phi\cos\theta\dot{\phi}\dot{\psi} - \sin\phi\dot{\phi}\dot{\theta}) - (I_{zz} - I_{xx})(\dot{\phi} - \sin\theta\dot{\psi})(\cos\phi\cos\theta\dot{\psi} - \sin\phi\dot{\theta}), \tag{6b}$$

$$M_z = I_{zz}(\cos\phi\cos\theta\ddot{\psi} - \sin\phi\ddot{\theta} - \cos\theta\sin\phi\dot{\phi}\dot{\psi} - \cos\phi\dot{\phi}\dot{\theta} - \cos\phi\sin\theta\dot{\psi}\dot{\theta}) - (I_{xx} - I_{yy})(\dot{\phi} - \sin\theta\dot{\psi})(\cos\phi\dot{\theta} + \sin\phi\cos\theta\dot{\psi}). \tag{6c}$$

Moments on the body are due to the normal force F_n, the friction force $F_\mu = \mu F_n$, and stiffness k's and damping b's acting about the three axes. These moments can be expressed in the xyz co-ordinate system as

$$M_x = F_n\{\mu[h_y(\sin\phi\sin\psi + \cos\phi\sin\theta\cos\psi) + h_z(\cos\phi\sin\psi - \sin\phi\sin\theta\cos\psi)] - h_y\cos\phi\cos\theta + h_z\cos\theta\sin\phi\} - k_\phi\phi - b_\phi\dot{\phi}, \tag{7a}$$

$$M_y = F_n\{\mu[h_x(\sin\phi\sin\psi + \cos\phi\sin\theta\cos\psi) + h_z\cos\theta\cos\psi] - h_x\cos\phi\cos\theta + h_z\sin\theta\} - k_\theta\theta - b_\theta\dot{\theta}, \tag{7b}$$

$$M_z = F_n\{\mu[h_x(\cos\phi\sin\psi - \sin\phi\sin\theta\cos\psi) - h_y\cos\theta\cos\psi] + h_x\cos\theta\sin\phi - h_y\sin\theta\} - k_\psi\psi - b_\psi\dot{\psi}, \tag{7c}$$

where F_n is given in equation (3).

By equating the right-hand sides of equations (6) and (7) and then rearranging, we obtain the equations of motion for the slider of Figure 1 in terms of variables θ, ϕ, ψ, which are a set of three second-order, *implicit ordinary differential equations.*

2.2. VERIFICATION

With special constraints, the 3-D model degenerates into Swayze and Akay's [14] 2-D model. The d.o.f. will reduce from four to two: two of the three Euler angles (ψ and a second angle) and their first and second time derivatives (which, in fact, are angular velocity and acceleration) will be zero. Four possible ways in which the 3-D model could be reduced were investigated to verify formulations, but only Case I is shown mathematically. The other three, which are listed, gave similar results.

Case I. The slider can rotate only about the y-axis, with the counter surface translating along the X direction.

For this, $\phi, \dot{\phi}, \ddot{\phi} = 0$, and equation (3) becomes

$$F_n = F_{st} - k_z(h_z - h_z\cos\theta - h_x\sin\theta) - b_z(h_z\sin\theta\dot{\theta} - h_x\cos\theta\dot{\theta})$$

$$- m[(h_z\sin\theta - h_x\cos\theta)\ddot{\theta} + (h_x\sin\theta + h_z\cos\theta)\dot{\theta}^2]. \tag{8}$$

Substituting $\phi, \dot{\phi}, \ddot{\phi} = 0$ and $\psi, \dot{\psi}, \ddot{\psi} = 0$, into equations (6) and (7), equating, and letting $h_y \to 0$ (to eliminate the third dimension) yields

$$I_{yy}\ddot{\theta} = F_n[\mu(h_x\sin\theta + h_z\cos\theta) - h_x\cos\theta + h_z\sin\theta] - k_\theta\theta - b_\theta\dot{\theta}. \tag{9}$$

Equations (8) and (9) are identical to equations (4) and (5) in reference [14].

Case II. The slider of Case I reoriented 90° so that it rotates about the x-axis with the counter surface still moving along the X direction.

Case III. The slider rotates only about the x-axis with the surface moving along the Y direction.

Case IV. Same as Case III, with the slider reoriented 90° so that it can rotate only about the y-axis.

3. NON-DIMENSIONALIZATION OF EQUATIONS

To facilitate solution of the system of differential equations implied by equations (6) and (7), we define the following dimensionless variables:

Natural frequencies: $\omega_z^2 = k_z/m$, $\omega_\phi^2 = k_\phi/I_{xx}$, $\omega_\theta^2 = k_\theta/I_{yy}$, and $\omega_\psi^2 = k_\psi/I_{zz}$.
Frequency ratios: $\Omega_\phi = \omega_\phi/\omega_z$, $\Omega_\theta = \omega_\theta/\omega_z$, and $\Omega_\psi = \omega_\psi/\omega_z$.
Damping ratios: $\zeta_z = b_z/2m\omega_z$, $\zeta_\phi = b_\phi/2I_{xx}\omega_\phi$, $\zeta_\theta = b_\theta/2I_{yy}\omega_\theta$, $\zeta_\psi = b_\psi/2I_{zz}\omega_\psi$.
Length ratios: $\alpha = h_x/h_z$, $\beta = h_y/h_z$.
Inertia ratios: $\gamma = mh_z^2/I_{xx} = 3/(\beta^2 + 1)$, $\lambda = mh_z^2/I_{yy} = 3/(\alpha^2 + 1)$, $\eta = mh_z^2/I_{zz} = 3/(\alpha^2 + \beta^2)$
Dimensionless time: $\tau = t\omega_z$.
Derivatives with respect to τ are indicated by "prime", $(\,)'$, i.e. $(\dot{\ }) = \omega_z(\,)'$.
Non-dimensional forces: $\bar{F}_n = F_n/m\omega_z^2h_z$, $\bar{F}_{st} = F_{st}/m\omega_z^2h_z$, $\bar{F}_{wav} = F_{wav}/m\omega_z^2h_z$.

With these definitions, we can write equations (6) as

$$\frac{M_x}{I_{xx}\omega_z^2} = \phi'' - \sin\theta\psi'' - \cos\theta\psi'\theta' - \gamma\left(\frac{1}{\lambda} - \frac{1}{\eta}\right)(\cos\theta\sin\phi\psi' + \cos\phi\theta')$$

$$\times(\cos\phi\cos\theta\psi' - \sin\phi\theta'), \tag{10a}$$

$$\frac{M_y}{I_{yy}\omega_z^2} = \cos\phi\theta'' + \cos\theta\sin\phi\psi'' - \sin\phi\sin\theta\psi'\theta' + \cos\phi\cos\theta\phi'\psi' - \sin\phi\phi'\theta'$$

$$- \lambda\left(\frac{1}{\eta} - \frac{1}{\gamma}\right)(\phi' - \sin\theta\psi')(\cos\phi\cos\theta\psi' - \sin\phi\theta'), \tag{10b}$$

$$\frac{M_z}{I_{zz}\omega_z^2} = \cos\phi\cos\theta\psi'' - \sin\phi\theta'' - \cos\theta\sin\phi\phi'\psi' - \cos\phi\phi'\theta' - \cos\phi\sin\theta\psi'\theta'$$

$$- \eta\left(\frac{1}{\gamma} - \frac{1}{\lambda}\right)(\phi' - \sin\theta\psi')(\cos\theta\sin\phi\psi' + \cos\phi\theta'). \tag{10c}$$

The total external moments in equation (7) can be expressed in the non-dimensional forms

$$\bar{M}_x = \frac{\Sigma M_x}{I_{xx}\omega_z^2} = \gamma \bar{F}_n\{\mu[\beta(\sin\phi\sin\psi + \cos\phi\sin\theta\cos\psi) + (\cos\phi\sin\psi - \sin\phi\sin\theta\cos\psi)] - \beta\cos\phi\cos\theta + \cos\theta\sin\phi\} - \Omega_\phi^2\phi - 2\zeta_\phi\Omega_\phi\phi', \tag{11a}$$

$$\bar{M}_y = \frac{\Sigma M_y}{I_{yy}\omega_z^2} = \lambda \bar{F}_n\{\mu[\alpha(\sin\phi\sin\psi + \cos\phi\sin\theta\cos\psi) + \cos\theta\cos\psi] - \alpha\cos\phi\cos\theta + \sin\theta\} - \Omega_\theta^2\theta - 2\zeta_\theta\Omega_\theta\theta', \tag{11b}$$

$$\bar{M}_z = \frac{\Sigma M_z}{I_{zz}\omega_z^2} = \eta \bar{F}_n\{\mu[\alpha(\cos\phi\sin\psi - \sin\phi\sin\theta\cos\psi) - \beta\cos\theta\cos\psi] + \alpha\cos\theta\sin\phi - \beta\sin\theta\} - \Omega_\psi^2\psi - 2\zeta_\psi\Omega_\psi\psi' \tag{11c}$$

and the normal force as

$$\begin{aligned}\bar{F}_n = \bar{F}_{st} &- (1 - \cos\phi\cos\theta - \beta\cos\theta\sin\phi - \alpha\sin\theta) \\ &- 2\zeta_z(\cos\phi\sin\theta\theta' + \cos\theta\sin\phi\phi' - \beta\cos\phi\cos\theta\phi' - \alpha\cos\theta\theta' \\ &+ \beta\sin\phi\sin\theta\theta') - [(\sin\phi\cos\theta - \beta\cos\phi\cos\theta)\phi'' + (\cos\phi\sin\theta \\ &+ \beta\sin\phi\sin\theta - \alpha\cos\theta)\theta'' + (\cos\phi\cos\theta + \beta\cos\theta\sin\phi)(\phi')^2 \\ &+ (\alpha\sin\theta + \beta\cos\theta\sin\phi + \cos\phi\cos\theta)(\theta')^2 + 2(\beta\cos\phi\sin\theta \\ &- \sin\phi\sin\theta)\phi'\theta'] \end{aligned} \tag{12}$$

Equating equation (10) with equation (11) and substituting $\bar{F}_n$ from Equation (12) into Equation (11) yields a set of very long and complicated non-linear ordinary differential equations. To simplify, we introduce new variables and rearrange the equations.

We define c_x, c_y, c_z, d_x, d_y, and d_z such that equations (11) assumes the form

$$\bar{M}_x = c_x\bar{F}_n + d_x,\ \bar{M}_y = c_y\bar{F}_n + d_y,\ \bar{M}_z = c_z\bar{F}_n + d_z, \tag{13a–c}$$

where c_x, c_y, and c_z are functions of (ϕ, θ, ψ), and that d_x, d_y, and d_z are functions of $(\phi, \phi', \theta, \theta', \psi, \psi')$.

We define a_ϕ, a_ϕ and $\hat{F}_n$ such that

$$\bar{F}_n = -a_\phi\phi'' - a_\theta\theta'' + \hat{F}_n, \tag{14}$$

where a_ϕ and a_θ are functions of (ϕ, θ).

Now equating equation (10) with equation (13), substituting $\bar{F}_n$ from equation (14), and rearranging terms, we obtain

$$(a_\phi c_x + 1)\phi'' + a_\theta c_x \theta'' - \sin\theta\psi''$$
$$= \gamma\left(\frac{1}{\lambda} - \frac{1}{\eta}\right)(\cos\theta\sin\phi\psi' + \cos\phi\theta')(\cos\phi\cos\theta\psi' - \sin\phi\theta')$$
$$+ \cos\theta\psi'\theta' + c_x\hat{F}_n + d_x. \tag{15a}$$

$$a_\phi c_y\phi'' + (a_\theta c_y + \cos\phi)\theta'' + \cos\theta\sin\phi\psi''$$
$$= \lambda\left(\frac{1}{\eta} - \frac{1}{\gamma}\right)(\phi' - \sin\theta\psi')(\cos\phi\cos\theta\psi' - \sin\phi\theta')$$
$$- (\cos\phi\cos\theta\phi'\psi' - \sin\phi\sin\theta\psi'\theta' - \sin\phi\phi'\theta') + c_y\hat{F}_n + d_y, \tag{15b}$$

$$a_\phi c_z\phi'' + (a_\theta c_z - \sin\phi)\theta'' + \cos\phi\cos\theta\psi''$$
$$= \eta\left(\frac{1}{\gamma} - \frac{1}{\lambda}\right)(\phi' - \sin\theta\psi')(\cos\theta\sin\phi\psi' + \cos\phi\theta')$$
$$+ \cos\theta\sin\phi\phi'\psi' + \cos\phi\phi'\theta' + \cos\phi\sin\theta\psi'\theta' + c_z\hat{F}_n + d_z. \tag{15c}$$

With appropriate initial conditions, equations (15) define the initial-value problem.

Note that we established the equations of motion only for $\phi, \theta > 0$, when the contact point is at the co − ordinate $(-h_x, h_y, h_z)$. For other cases, the equations are valid if the signs of length ratios α and β change as follows: when $\phi < 0$: $\beta = -h_y/h_z$; when $\theta < 0$: $\alpha = -h_x/h_z$.

4. STABILITY ANALYSIS

To ascertain the stability of the system (15) for possible design of vibrating sliders, we will determine all equilibrium points of these equations, along with their relative stability. Our procedure will follow Swayze and Akay [14]. The equilibrium points ϕ_e, θ_e, and ψ_e can be determined by setting all derivative terms in equation (15) to zero, and then solving the set of resulting transcendental equations. With derivative terms zero, equations (15) become

$$0 = \gamma\bar{F}_{ne}\{\mu[\beta(\sin\phi_e\sin\psi_e + \cos\phi_e\sin\theta_e\cos\psi_e) + (\cos\phi_e\sin\psi_e$$
$$- \sin\phi_e\sin\theta_e\cos\psi_e)] - \beta\cos\phi_e\cos\theta_e + \cos\theta_e\sin\phi_e\} - \Omega_\phi^2\phi_e, \tag{16a}$$

$$0 = \lambda\bar{F}_{ne}\{\mu[\alpha(\sin\phi_e\sin\psi_e + \cos\phi_e\sin\theta_e\cos\psi_e) + \cos\theta_e\cos\psi_e]$$
$$- \alpha\cos\phi_e\cos\theta_e + \sin\theta_e\} - \Omega_\theta^2\theta_e, \tag{16b}$$

$$0 = \eta\bar{F}_{ne}\{\mu[\alpha(\cos\phi_e\sin\psi_e - \sin\phi_e\sin\theta_e\cos\psi_e) - \beta\cos\theta_e\cos\psi_e]$$
$$+ \alpha\cos\theta_e\sin\phi_e - \beta\sin\theta_e\} - \Omega_\psi^2\psi_e, \tag{16c}$$

where

$$\bar{F}_{ne} = \bar{F}_{st} - (1 - \cos\phi_e\cos\theta_e - \beta\sin\phi_e\cos\theta_e - \alpha\sin\theta_e).$$

Equations (16) comprise three equations in three unknowns ϕ_e, θ_e, and ψ_e which can be solved numerically. Due to the non-linear functions, there may exist multiple equilibrium points or none at all, depending on the values of the parameters. Equation (16) is only valid for $\phi, \theta > 0$; candidate solutions ϕ_e or θ_e cannot violate this condition. For the other cases, sign changes of α and β must be consistent with the criteria given above.

Because of the piecewise nature of the equations of motion, the preceding analysis will fail when ϕ or $\theta = 0$. These points are physically important since most bodies begin with zero displacement. We apply a potential energy analysis instead.

Neglecting gravity, the potential energy V of the system is

$$V = \tfrac{1}{2}(k_\phi \phi^2 + k_\theta \theta^2 + k_\psi \psi^2 + k_z Z^2) - F_{st} Z, \tag{17}$$

where $Z \leqslant 0$ is the vertical displacement due to small angular rotations given in equation (1). Since $F_{st} \geqslant 0$, potential energy $V \geqslant 0$, so

$$F_{st} Z \geqslant \tfrac{1}{2}(k_\phi \phi^2 + k_\theta \theta^2 + k_\psi \psi^2 + k_z Z^2).$$

By dividing both sides by $mh_z^2\omega_z^2$, equation (17) can be written in the non-dimensional form

$$\bar{V} = \frac{V}{mh_z^2\omega_z^2} = \frac{1}{2}\left(\frac{\Omega_\phi^2}{\gamma}\phi^2 + \frac{\Omega_\theta^2}{\lambda}\theta^2 + \frac{\Omega_\psi^2}{\eta}\psi^2 + \bar{Z}^2\right) - \bar{F}_{st}\bar{Z}, \tag{18}$$

where

$$\bar{Z} = \frac{Z}{h_z} = -\left[\alpha \sin\theta + \beta \sin\phi \cos\theta - (1 - \cos\phi \cos\theta)\right].$$

The relative minima, relative maxima, and points of reflection of V represent equilibrium points. Relative minima correspond to centers that are stable; relative maxima correspond to saddle points that are not. The potential energy V depends on ϕ, θ, and ψ. The piecewise nature of the equations of motion, however, pertains to ϕ and θ, but not ψ. Hence, we hold ψ constant and plot V versus ϕ and θ. Figure 2 shows an example when $\phi, \theta > 0$. The surface for V in the other three quadrants could be constructed by symmetries about the $\phi = 0$ plane, the $\theta = 0$ plane, and the origin. From this analysis, the potential energy has a local minimum at $\phi, \theta = 0$ and the system is stable about this point. Numerical

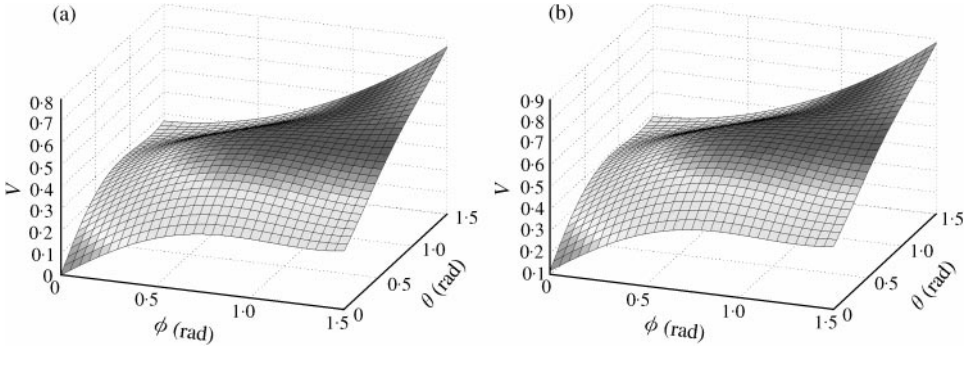

Figure 2. Potential energy of the system versus ϕ and θ; $\bar{F}_{st} = 0{\cdot}9$, $\alpha = \beta = 0{\cdot}6$, $\Omega_\phi = \Omega_\theta = \Omega_\psi = 1{\cdot}0$, $\zeta_z = \zeta_\phi = \zeta_\theta = \zeta_\psi = 0$, $\mu = 0{\cdot}0$: (a) $\psi = 0{\cdot}0$ rad; (b) $\psi = 1{\cdot}0$ rad.

simulations support this argument. Another interesting point observed during simulations is that different values of ψ shift the potential energy surface up or down, and seem not to affect the shape of the surface.

This model is based on the assumption that all rotations ϕ, θ, and ψ are small and can be considered commutative. The system has been shown stable about $\phi, \theta = 0$. An important question is "For how large a region about $\phi, \theta = 0$ is the system still stable?" and "How do system parameters affect stability?"

System parameters influencing stability include μ, α, β, Ω_ϕ, Ω_θ, Ω_ψ, ζ_z, ζ_ϕ, ζ_θ, ζ_ψ, and $\bar{F}_{st}$. As verified earlier, when $\beta = 0$, the model is identical to Swayze and Akay's whose stability "analysis was covered in reference [14]. Our discussions will focus on stability when $\beta \neq 0$, using Swayze and Akay's approach as a guide.

An important parameter is the coefficient of friction. Larger values shrink the domain of attraction of the stable point at the origin which remains a stable equilibrium point as long as the coefficient of friction does not exceed a critical value μ_{cr}. For $\mu > \mu_{cr}$, stability depends on other parameters such as stiffnesses and static force $\bar{F}_{st}$. We used Swayze and Akay's approach to determine μ_{cr} and found that $\mu_{cr} = \alpha$. Figure 3 illustrates how the coefficient of friction influences the system response. In Figures 3(a)–3(c), where $\mu < \mu_{cr}$, the system has an equilibrium point at $\theta = 0$. In Figure 3(d), where $\mu > \mu_{cr}$, instead of the origin, the system has an equilibrium point about $\theta = 1{\cdot}0$. Excessive friction tends to tilt the slider.

Increases in the static normal force $\bar{F}_{st}$ seem to decrease the domain of attraction of the stable point at the origin. Figure 4 contains simulations of rotations (ϕ, θ, ψ) versus non-dimensional time τ, with parameters $\bar{F}_{st}$, Ω_ϕ, Ω_θ, and Ω_ψ varied. By comparing the sub-figures of Figure 4, it is seen that excessive $\bar{F}_{st}$ could cause instability when $\mu \geq \mu_{cr}$. In Figure 4(b), the maximum magnitudes of ϕ and ψ are approximately 7 and 14 rad, respectively. Therefore, it is desirable to keep $\bar{F}_{st}$ as low as possible. Large values of the natural frequency ratios, Ω_ϕ, Ω_θ, and Ω_ψ, associated with torsional stiffnesses, improve stability, or provide stability for a system otherwise unstable, as illustrated in Figure 4. The Figure 5 plots are similar to those in Figure 4, except that damping is increased and friction coefficient μ is varied. Damping does not change the position of the equilibrium point but causes the response to eventually decay to the equilibrium point, which usually improves stability.

Similar observations of the effects of these system parameters were also noticed by Swayze and Akay in their two-dimensional model [14].

In York's experiments [12], the slider was held within a holder, limiting its rotations to a maximum of approximately $\pm 10^{-2}$ rad. As stated earlier, the slider has a stable equilibrium point at $\phi, \theta = 0$. However, there might be other stable equilibrium points within the range of $\pm 10^{-2}$ rad. To determine equilibrium points, we solve equation (16) numerically with the following parameter values: $\alpha = \beta = 0{\cdot}2$, $\mu = 0{\cdot}25$, $\bar{F}_{st} = 2{\cdot}0$, $\Omega_\phi = \Omega_\theta = \Omega_\psi = 40$. All candidate solutions found violated the condition $\phi_e, \theta_e > 0$. However, simulations suggested a stable equilibrium point at $\theta \neq 0$, $\phi = 0$ (see Figure 6) although the equilibrium point could not be found by solving equation (16), invalid when $\phi = 0$. Even though the potential energy surfaces in Figure 2 are for another set of parameters, they suggest that, along plane $\phi = 0$, there are possible points where $\partial V/\partial\theta = 0$ and thus minima.

5. SIMULATION RESULTS

Equations (15) were solved by a numerical solver [16, 17] that employs a modified divided difference form of the Adams–Bashforth–Moulton family of orders 1–12. For most

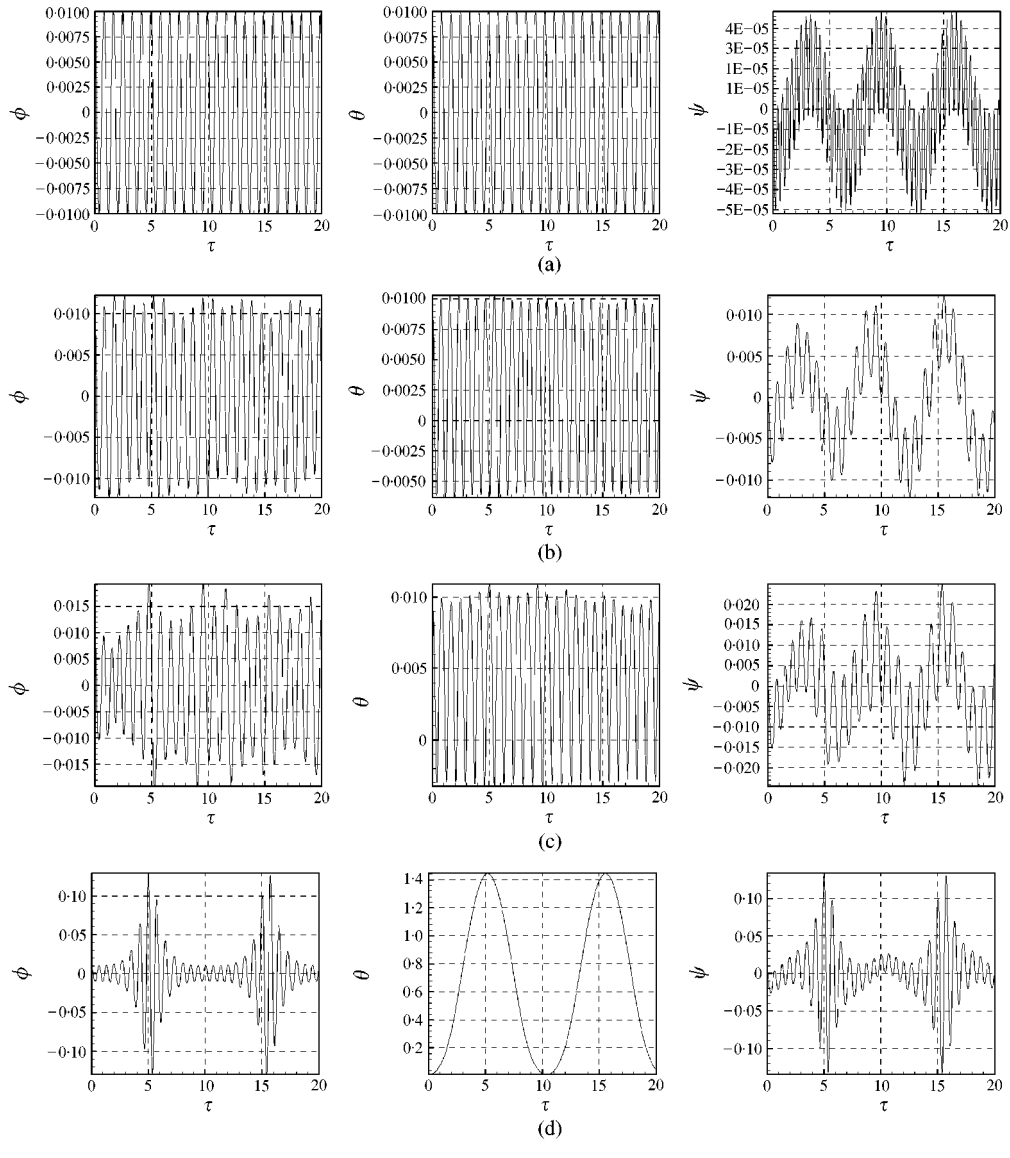

Figure 3. System responses for different coefficients of friction; $\bar{F}_{st} = 0{\cdot}9$, $\alpha = \beta = 0{\cdot}6$, $\Omega_\phi = \Omega_\theta = \Omega_\psi = 1{\cdot}0$, and $\zeta_z = \zeta_\phi = \zeta_\theta = \zeta_\psi = 0$: (a) $\mu = 0{\cdot}0$; (b) $\mu = 0{\cdot}2$; (c) $\mu = 0{\cdot}4$; (d) $\mu = 0{\cdot}7$.

calculations, 10^{-6} and 10^{-8} were used for the relative error tolerance and absolute error tolerance respectively.

5.1. NUMERICAL VERIFICATION

To simulate Swayze and Akay's [14] results numerically (to increase confidence in the numerical method), we must restrict rotations to one d.o.f (θ angle), and enforce a two-dimensional model with an infinitesimally thin thickness. With $\beta \to 0$, our model approaches Swayze and Akay's, and regardless of the values of Ω_ϕ and Ω_ψ, the simulations

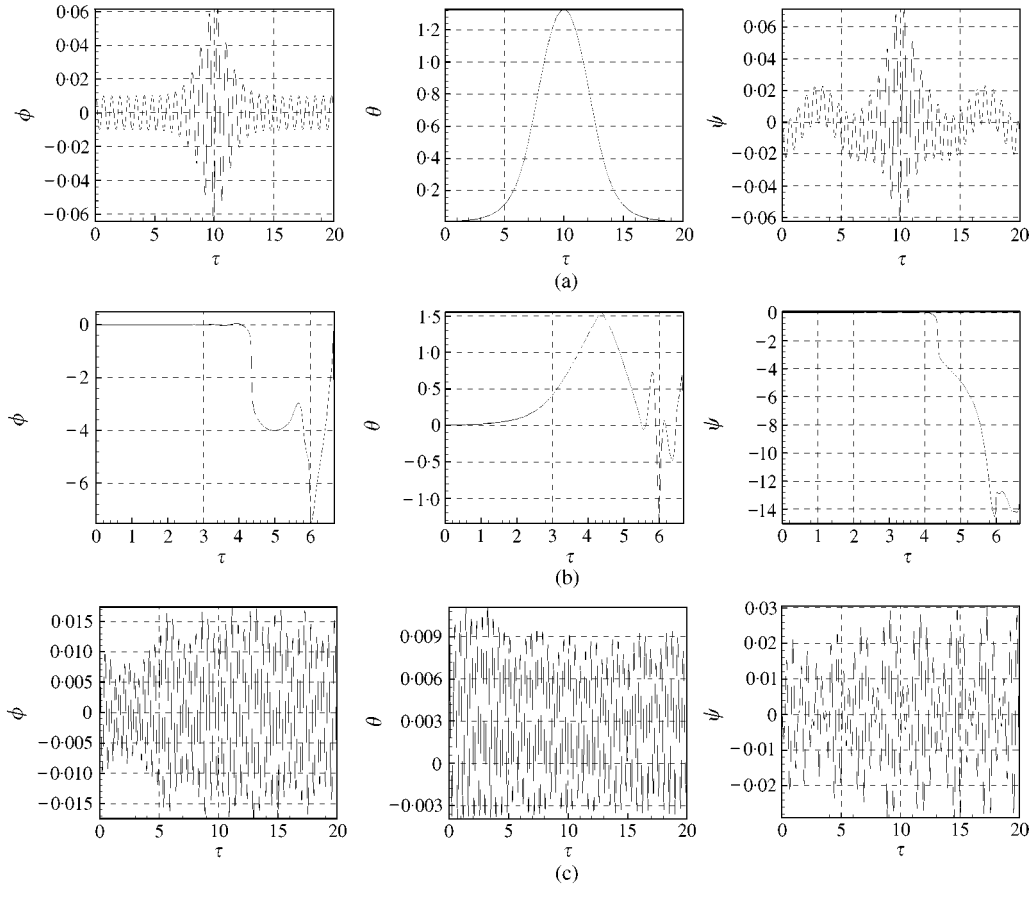

Figure 4. Increase in $\bar{F}_{st}$ might cause instability and increase in Ω_ϕ, Ω_θ, and Ω_ψ improves stability; $\mu = 0{\cdot}6$, $\alpha = \beta = 0{\cdot}6$, and $\zeta_z = \zeta_\phi = \zeta_\theta = \zeta_\psi = 0$: (a) $\bar{F}_{st} = 0{\cdot}9$ and $\Omega_\phi = \Omega_\theta = \Omega_\psi = 1{\cdot}0$; (b) $\bar{F}_{st} = 2{\cdot}0$ and $\Omega_\phi = \Omega_\theta = \Omega_\psi = 1{\cdot}0$; (c) $\bar{F}_{st} = 2{\cdot}0$ and $\Omega_\phi = \Omega_\theta = \Omega_\psi = 10{\cdot}0$.

perfectly match Swayze and Akay's Figures 4(a) and 4(c) in reference [14]. The motions in the other two d.o.f, i.e. $\phi, \dot{\phi}, \psi$ and $\dot{\psi}$, remain identically zero, because when $\beta = 0$, the differential equations are decoupled.

When $\beta \neq 0$, results deviate monotonically from Swayze and Akay's. Phase plane plots of Figure 7 show the simulations of two randomly chosen cases for $\beta =$ 0·01, 0·1, 1, and 10 times α ($\beta = 0$ is also included for comparison) with $\Omega_\phi, \Omega_\psi = 1$ for every β. As can be seen for Figure 7, for larger β the size of the closed trajectory in the phase plane grows.

5.2. SURFACE WAVINESS STUDY

5.2.1. *Introduction*

Past studies of slider rigid-body motions usually assume a *smooth* counter surface with one contact point between slider and counter surface. Real surfaces exhibit undulations extending in two directions with multiple contact points. We will replace the multiple contact points with an "equivalent" contact point applied by an equivalent force system

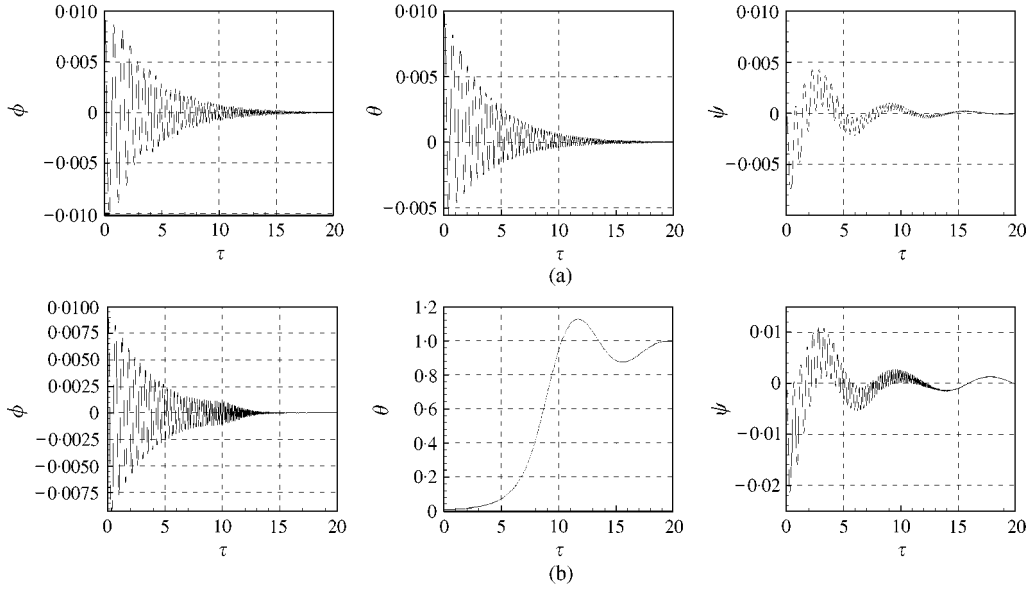

Figure 5. System responses decay to the equilibrium point with damping present; $\bar{F}_{st} = 0{\cdot}9$, $\alpha = \beta = 0{\cdot}6$, $\Omega_\phi = \Omega_\theta = \Omega_\psi = 1{\cdot}0$, and $\zeta_z = \zeta_\phi = \zeta_\theta = \zeta_\psi = 0{\cdot}2$: (a) $\mu = 0{\cdot}2$; (b) $\mu = 0{\cdot}6$.

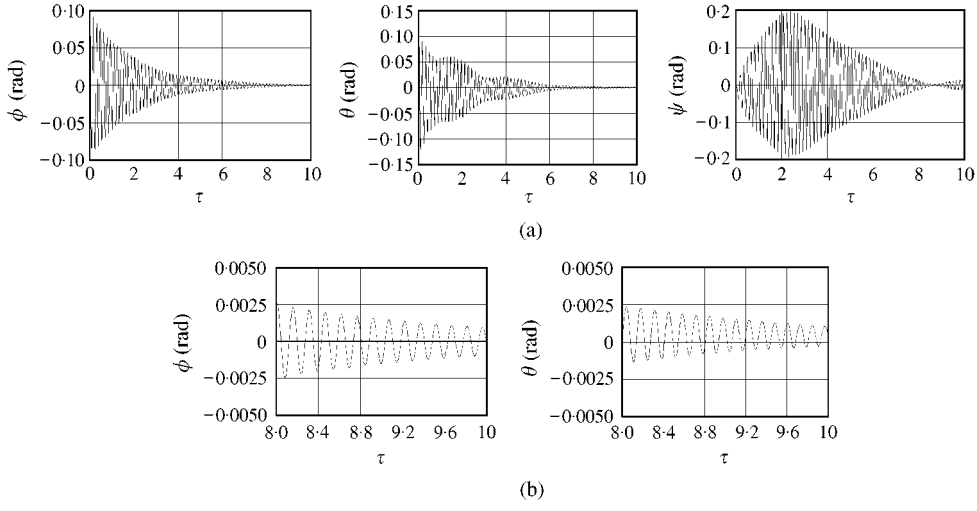

Figure 6. Equilibrium point is at $\phi = 0$ but $\theta \neq 0$; $\alpha = \beta = 0{\cdot}2$, $\mu = 0{\cdot}25$, $\bar{F}_{st} = 2{\cdot}0$, $\Omega_\phi = \Omega_\theta = \Omega_\psi = 40$, and $\zeta_z = \zeta_\phi = \zeta_\theta = \zeta_\psi = 0{\cdot}5$: (a) system responses; (b) magnified views of ϕ and θ responses at the end of the simulation.

with contact tractions (having forces and moments) equivalent to those generated by the multiple contact points.

Consider possible paths $\mathscr{P}(t)$ depicted in Figure 8 of the equivalent contact point moving across the slider's face. The path $\mathscr{P}(t)$ influences rigid-body motions of the slider via the forces and moments that the contact tractions at these various locations generate. As the counter surface moves beneath the slider, waviness of the counter surface causes the equivalent point to move about the slider's bottom surface. Let $(x(t), y(t))$ be a point in the path $\mathscr{P}(t) = \{(x(t), y(t)) : y = g(x) \text{ and } t \in (t_0, t_0 + T)\}$, where t_0 is some initial time and

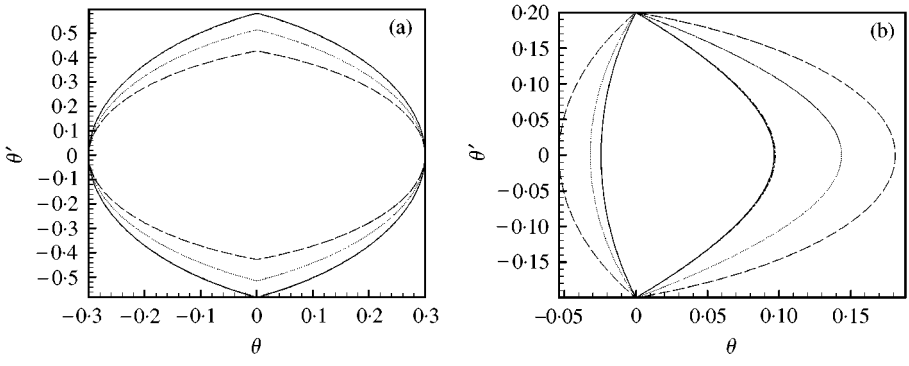

Figure 7. Phase plane plots when β varies; $\alpha = 1/1{\cdot}8$, $\bar{F}_{st} = 1{\cdot}5/\alpha$, $\Omega_\theta = \Omega_\phi = \Omega_\psi = 1{\cdot}0$. $\zeta_\theta = \zeta_\phi = \zeta_\psi = \zeta_z = 0{\cdot}0$. ——, $\beta = 0$; – – –, $\beta = 0{\cdot}01\alpha$; – · – · –, $\beta = 0{\cdot}1\alpha$; ·····, $\beta = \alpha$; ———, $\beta = 10\alpha$; parameters are in accordance with reference [14]. (a) $\mu = 0{\cdot}0$; (b) $\mu = 0{\cdot}4$.

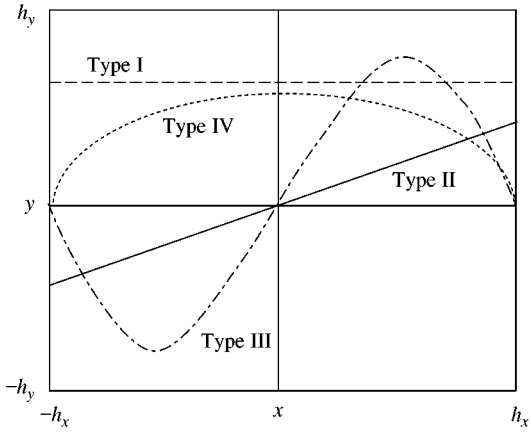

Figure 8. Four path types considered in the study. – – –, *Type I*; ——, *Type II*; – · –, *Type III*; ·····, *Type IV*.

T is the time the contact point traverses path $\mathscr{P}(t)$. To apply these concepts, the equivalent contact point must now be at $(x(t), y(t), h_z)$, instead of $(-h_x, h_y, h_z)$, in the xyz system. Thus, the equations of motion can be obtained by replacing $-h_x$ and h_y with $x(t)$ and $y(t)$ respectively, in all the equations of motion in section 2.1.

Possible path functions considered included (see Figure 8)

- *Type I*: straight line back with constant, $\mathrm{y} = A$;
- *Type II*: straight line angled with linear, $\mathrm{y} = A\mathrm{x}$;
- *Type III*: sinusoidal, $\mathrm{y} = A\sin(\omega\mathrm{x})$;
- *Type IV*: half-ellipse, $\mathrm{y} = A\sqrt{b^2 - \mathrm{x}^2}$. The path would become a half-circle when $A = 1$.

In practice, surface waviness on the counter surface generates the path of the equivalent contact point. On rotors, waviness profiles are periodic, with a period T equal to the time of one full rotation. To incorporate this, our equivalent contact point will repetitively sweep out paths $\mathscr{P}(t)$ over the slider face: $|\mathrm{x}| \leqslant h_x$ and $|\mathrm{y}| \leqslant h_y$ will be periodic functions of time with period T. In non-dimensional form, we define $\bar{\mathrm{x}} = \mathrm{x}/h_z$ and $\bar{\mathrm{y}} = \mathrm{y}/h_z$, so $|\bar{\mathrm{x}}| \leqslant \alpha$ and $|\bar{\mathrm{y}}| \leqslant \beta$.

5.2.2. *Results and discussions*

Typical responses (ϕ, θ, ψ) versus time τ, and spectral densities of these waveforms obtained via Fourier transformations, for path motions along the four path types *I–IV* are shown in Figures 9–13. Here, $\bar{x}(\tau) = \alpha \cos(2\pi\tau/\bar{T})$, where $\tau = t\omega_z$ is a dimensionless time defined in section 4, $\bar{T} = T\omega_z$ is the dimensionless period of $\bar{x}$, and f and $f\omega_z$ are the non-dimensional and dimensional frequencies. Parameters in the simulations were $\alpha = \beta = 0{\cdot}6$, $\mu = 0{\cdot}2$, $\bar{F}_{st} = 5{\cdot}0$, $\Omega_\phi = \Omega_\theta = \Omega_\psi = 100$, and $\zeta_z = \zeta_\phi = \zeta_\theta = \zeta_\psi = 0{\cdot}0$. The period $\bar{T}$ was varied, although for the typical data shown in Figures 9–13, $\bar{T} = 0{\cdot}1$. Results and details of other cases simulated can be found in reference [18].

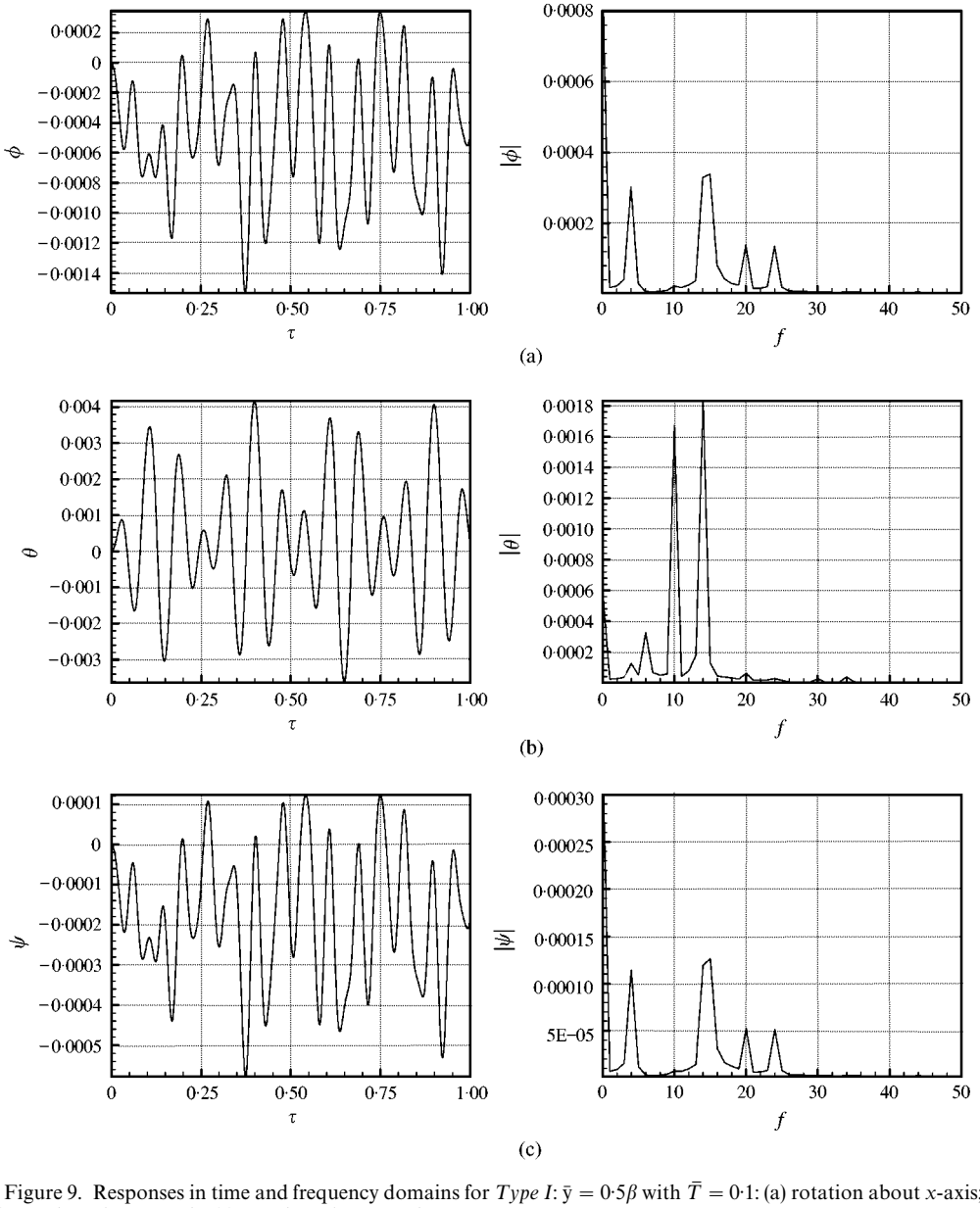

Figure 9. Responses in time and frequency domains for *Type I*: $\bar{y} = 0{\cdot}5\beta$ with $\bar{T} = 0{\cdot}1$: (a) rotation about *x*-axis; (b) rotation about *y*-axis; (c) rotation about *z*-axis.

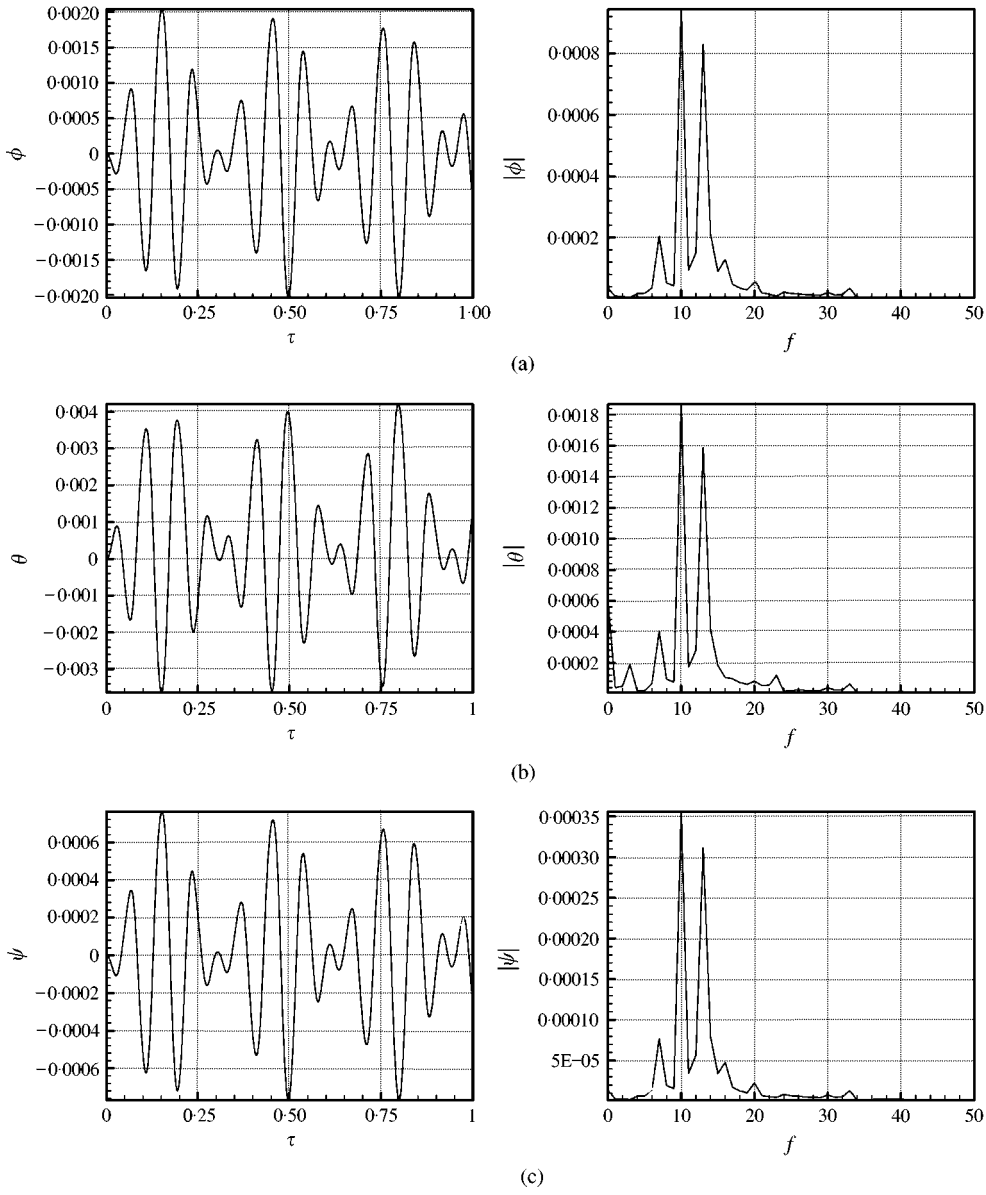

Figure 10. Responses in time and frequency domains for *Type II*: $\bar{y} = 0{\cdot}5\bar{x}$ with $\bar{T} = 0{\cdot}1$: (a) rotation about x-axis; (b) rotation about y-axis; (c) rotation about z-axis.

Figure 9 show typical responses for *Type I* paths with $\bar{y} = 0{\cdot}5\beta$. The θ trace contains the fundamental component at frequency $f = 10$, inverse to the period $\bar{T} = 0{\cdot}1$, and a second component near frequency $f = 14$, likely a natural frequency. Due to the closeness of the two components, a "beat" appears in the θ trace. The traces and spectra for ϕ and ψ were similar: both lacked the fundamental component, instead containing a component at twice the applied frequency, and their largest component was at the aforementioned natural frequency. At $\bar{T} = 0{\cdot}01$, the responses were greatly enhanced, suggesting another natural frequency. *Type I* paths with $\bar{y} = 0$ (where the equivalent contact point swept back and forth along the x-axis) gave $\phi = \psi = 0$. This was expected, since the path along the x-axis

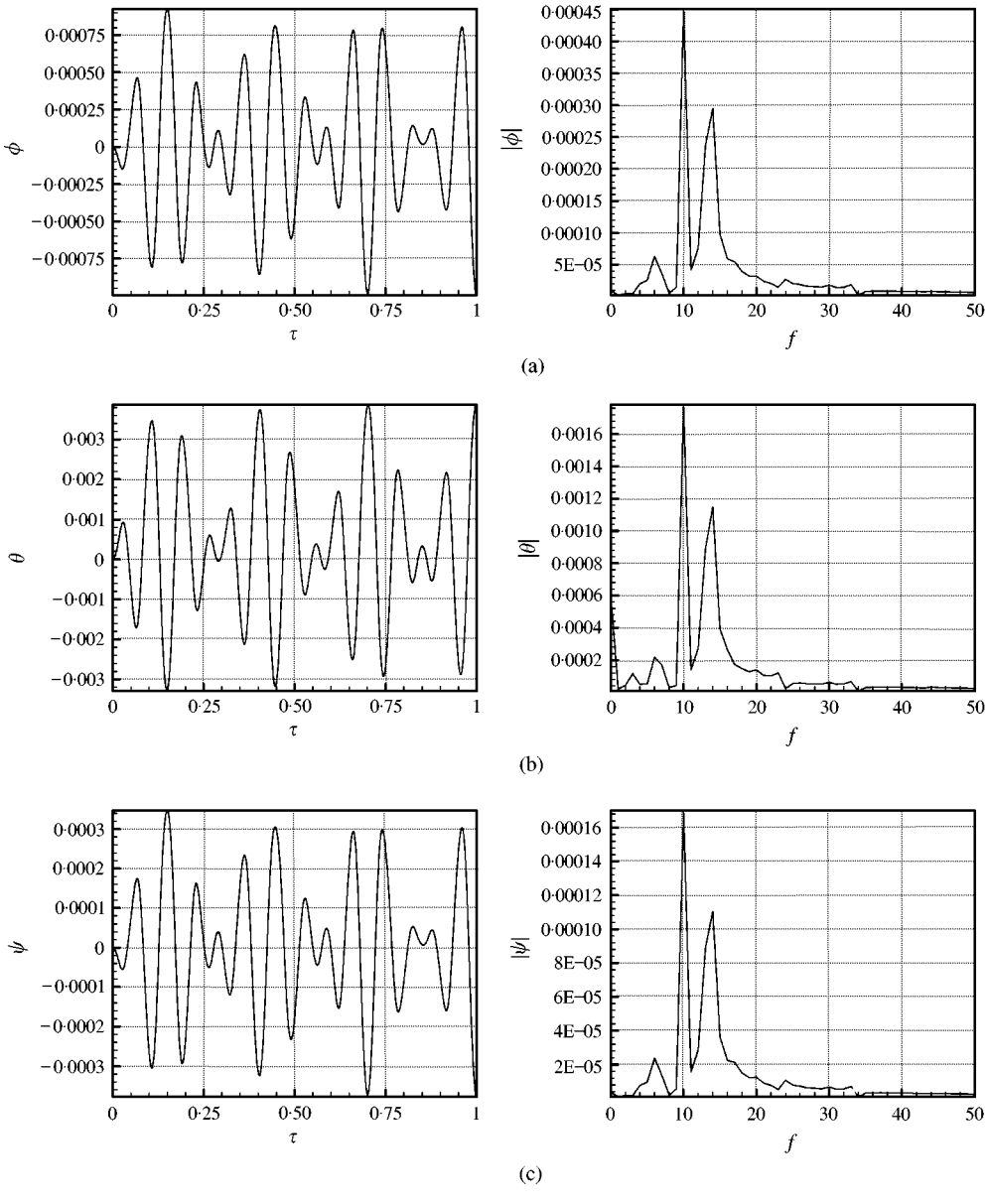

Figure 11. Responses in time and frequency domains for *Type II*: $\bar{y} = 0{\cdot}25\bar{x}$ with $\bar{T} = 0{\cdot}1$. (a) rotation about x-axis; (b) rotation about y-axis; (c) rotation about z-axis.

generated no moment to excite these degrees of freedom. Finally, for paths $\bar{y} = 0$ with periods $\bar{T} = 0{\cdot}01$, the component at $f = 14$ dominated the spectrum and the beat disappeared.

Responses for *Type II* paths with $\bar{y} = 0{\cdot}5\bar{x}$ and $\bar{y} = 0{\cdot}25\bar{x}$ are shown in Figures 10 and 11. Here the ϕ and ψ frequency spectra resemble the θ frequency spectrum. A component corresponding to the applied frequency now appears in ϕ and ψ. With $\bar{y} = 0{\cdot}25\bar{x}$, waveforms have similar shapes but reduced peak to peak values. At $\bar{T} = 0{\cdot}01$, components of frequencies ranging from 12 to 16 were prevalent, which encouraged beats.

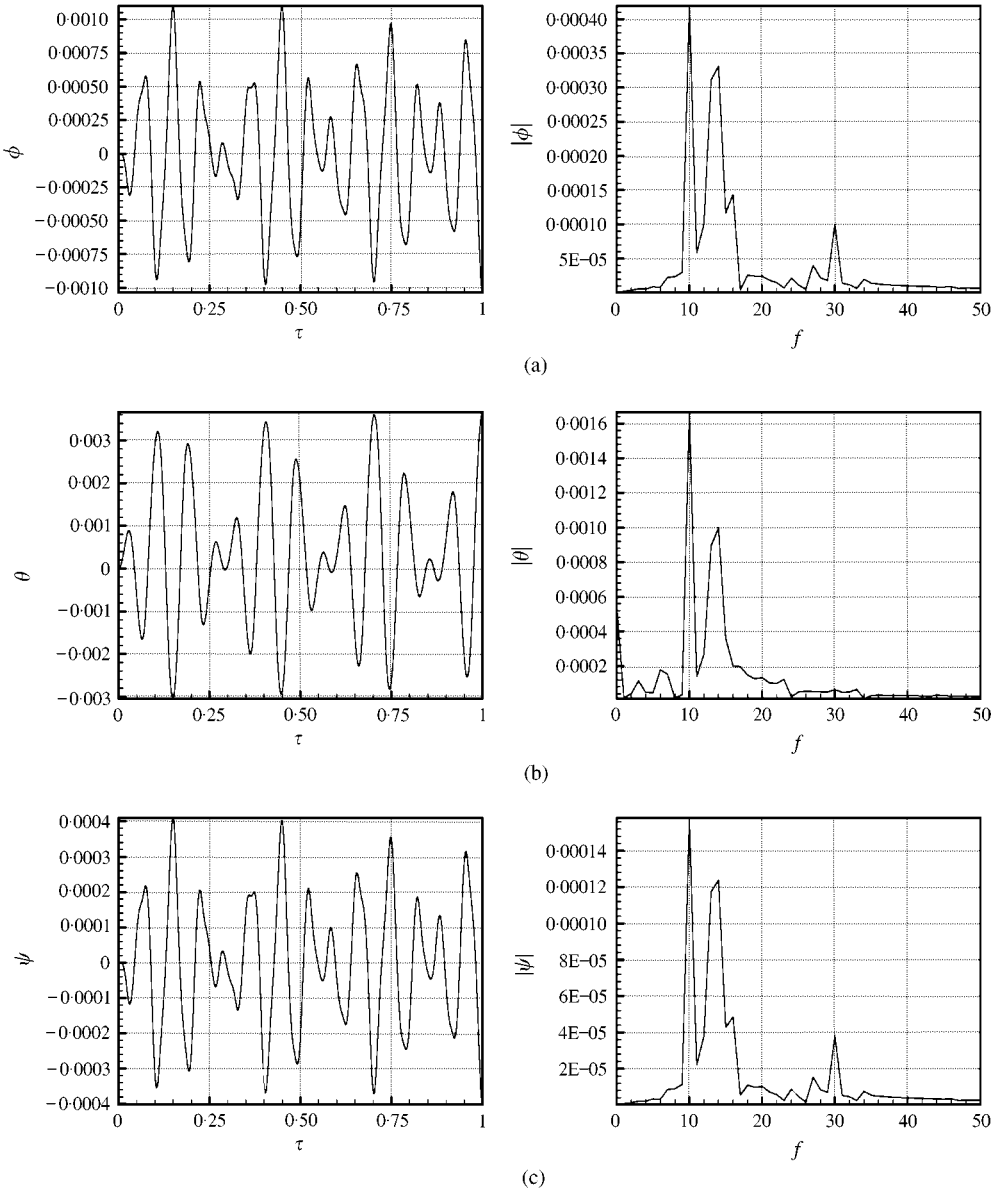

Figure 12. Responses in time and frequency domains for *Type III*: $\bar{y} = 0{\cdot}5\beta\sin(\pi\bar{x}/\alpha)$ with $\bar{T} = 0{\cdot}1$. (a) rotation about x-axis; (b) rotation about y-axis; (c) rotation about z-axis.

Figures 12 demonstrate responses for *Type III* paths with $\bar{y} = 0{\cdot}5\beta\sin(\pi\bar{x}/\alpha)$. The responses were similar to *Type II*, except for a frequency component at 30 in the ϕ and ψ responses, three times higher than the applied frequency. At $\bar{T} = 0{\cdot}2$ or $\bar{f}_x = 5$, the natural frequency component at 14 was increased, especially for ϕ and ψ.

As seen in Figures 13, for *Type IV* paths with $\bar{y} = 0{\cdot}5\beta\sqrt{(\alpha^2 - \bar{x}^2)}$, the overall responses are very similar to those of *Type I*, including the presence of the component at twice the applied frequency. At $\bar{T} = 0{\cdot}01$, however, the responses were not as enhanced.

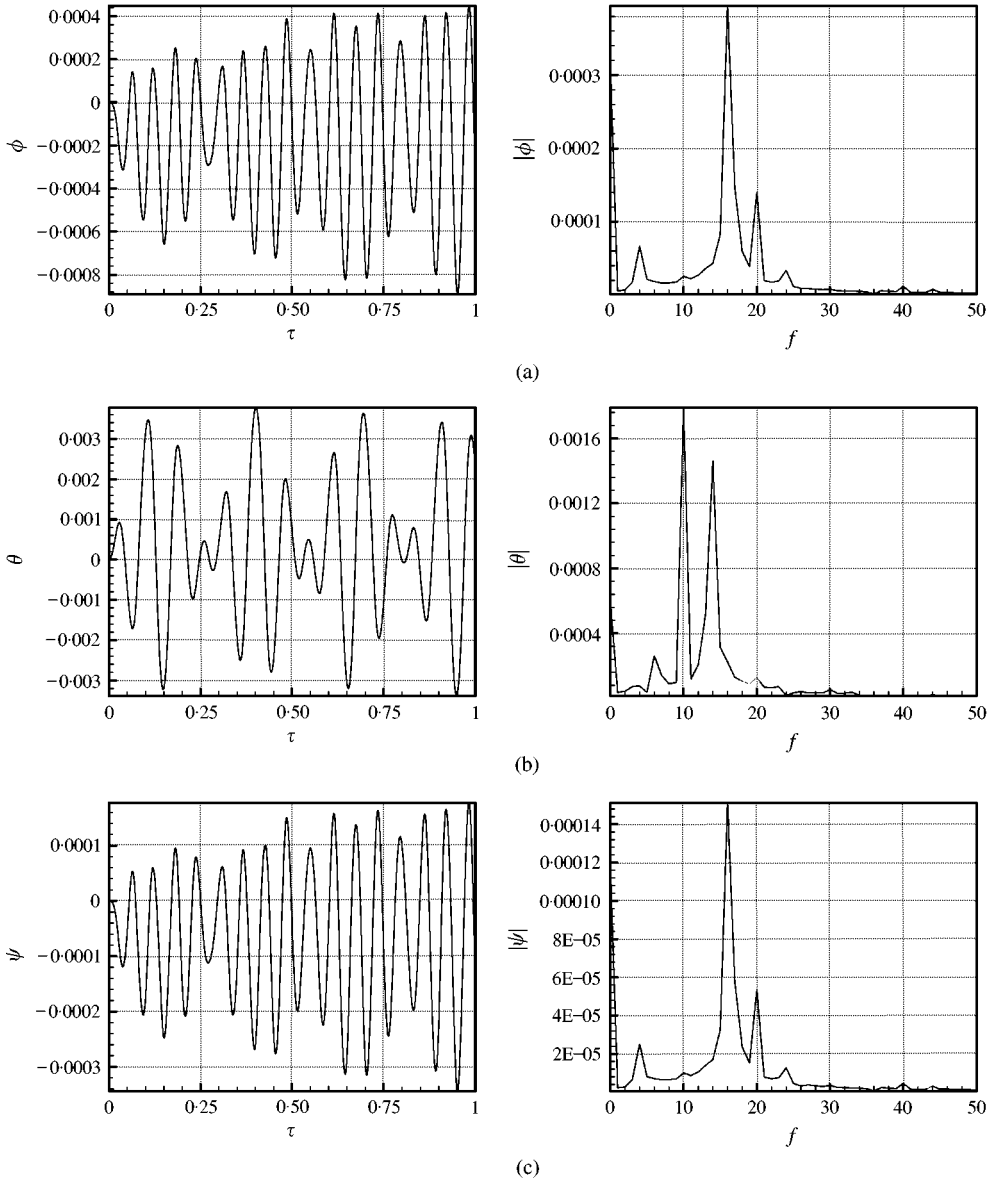

Figure 13. Responses in time and frequency domains for *Type IV*: $\bar{y} = 0{\cdot}5\beta\sqrt{(\alpha^2 - \bar{x}^2)}$ with $\bar{T} = 0{\cdot}1$. (a) rotation about x-axis; (b) rotation about y-axis; (c) rotation about z-axis.

The following conclusions can be drawn from Figures 9–13.

1. For a given period T, both magnitudes and frequency components of θ responses are similar for all the path types studied (cf. Figures 9–13). We conclude that θ responses depend strongly on $x(t)$, and weakly on the path function $y = g(x)$. For waviness wavelengths $s > 2h_x$, rotations θ (about the y-axis) are associated with tilting of the slider as it climbs and descends waviness hills in its path, which is directed along X.
2. ϕ and ψ responses depend on the path function $y = g(x)$, with magnitudes proportional to the magnitude of the path function at a given period. Waviness ridges

extending non-perpendicular to X would generate $y = g(x)$, and induce tilting ϕ of the body about the X axis. Rotations ψ are induced by the equivalent contact point acting at a distance from the z axis (see Figure 1). Compare Figures 10 and 11, where $y(x) = 0{\cdot}5x$ and $0{\cdot}25x$ respectively.

3. The overall responses for *Type I* and *Type IV* are similar, cf. Figures 9 and 13. The overall responses for *Type II* and *Type III* are also similar, cf. Figures 10 and 12.
4. System responses usually have a larger component at the natural frequency than the applied frequency.

5.2.3. *Comparisons with experimental results*

In the apparatus of reference [13], a $2{\cdot}46\ \text{cm} \times 2{\cdot}32\ \text{cm} \times 10\ \text{cm}$ carbon graphite block of 0.09 kg, spring loaded in a holder, slid against a rotor. Surface waviness passed beneath the slider (along X) with speed U, and forced the slider to translate normal to the sliding surface, and rock with rotation vectors parallel and perpendicular to the sliding direction. A capacitance gauge measured translations (X, Y, Z) shown in Figure 1; displacements X and Y were converted into rotations θ and ϕ, with rotation vectors parallel and perpendicular to the sliding direction X. Clearances between the slider and the holder limited motions of the sliders. A "snug fit" clearance restricted rigid-body translations (X, Y) of the slider to 50 μm or less, and consequently, rocking rotations θ and ϕ.

Figures 14(a) and 15(a), taken from reference [13], were measured during sliding on the same wavy surface. Figure 14(a) pertains to displacements Z normal to the counter surface,

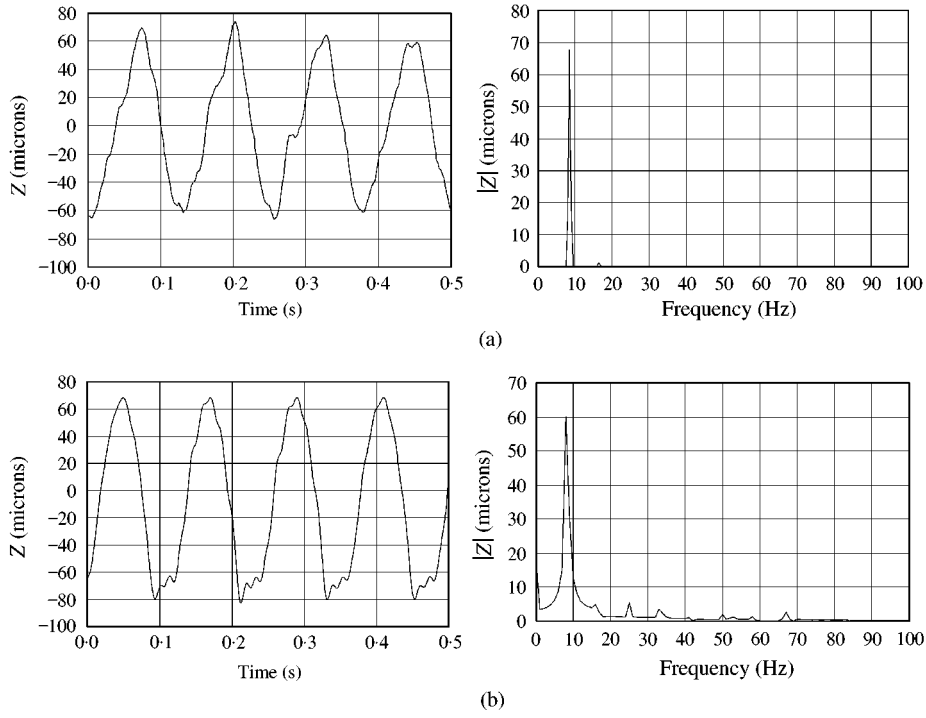

Figure 14. Similar responses in time and frequency domains from Bryant and York's experiments and the simulations using the proposed model: (a) Bryant and York's experimental conditions: Z vibrations, snug fit at 500 rpm (Figure 4(b) in reference [13]); (b) simulation parameters: Z vibrations, $T = 0{\cdot}12$, *Type II* path with $\bar{y} = 0{\cdot}8\bar{x}$, $\mu = 0{\cdot}2$, $\bar{F}_{st} = 2{\cdot}0$, $\Omega_\phi = \Omega_\theta = 40$, $\Omega_\psi = 100$, $\zeta_z = \zeta_\phi = \zeta_\theta = \zeta_\psi = 0{\cdot}3$

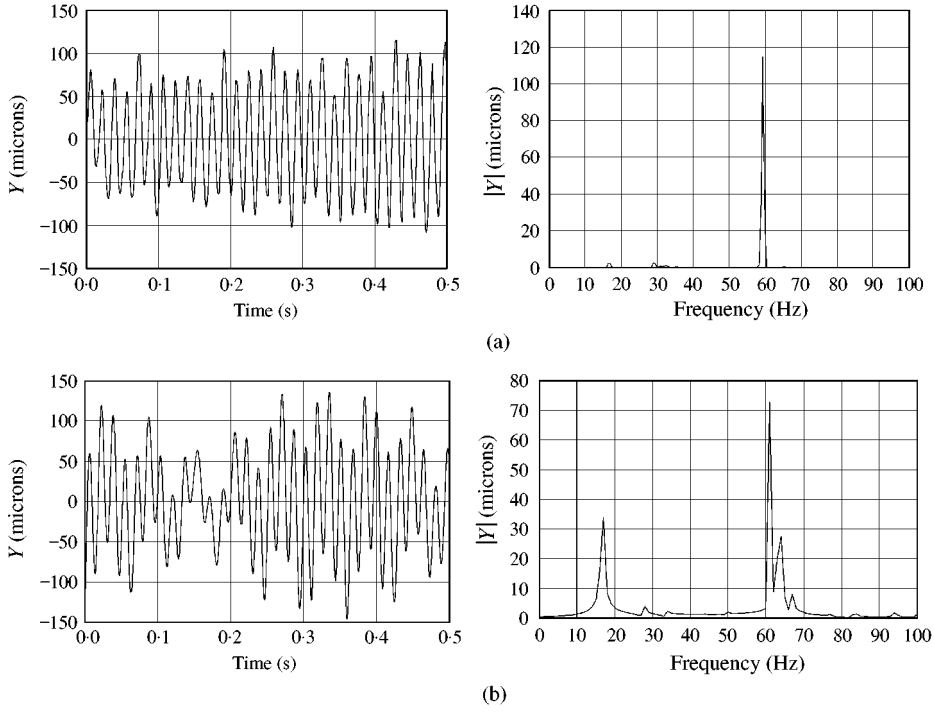

Figure 15. Similar responses in time and frequency domains from Bryant and York's experiments and the simulations using the proposed model. (a) Bryant and York's experimental conditions: Y vibrations, snug fit at 1000 rpm (Figure 4(b) in reference [13]); (b) simulation parameters: Y vibrations, $T = 0{\cdot}06$, *Type II* path with $\bar{y} = 0{\cdot}8\bar{x}$, $\mu = 0{\cdot}2$, $\bar{F}_{st} = 2{\cdot}0$, $\Omega_\phi = \Omega_\theta = 40$, $\Omega_\psi = 100$, $\zeta_z = \zeta_\phi = \zeta_\theta = \zeta_\psi = 0{\cdot}0$.

at a rotational speed of 500 rpm, which corresponds to sliding at $7{\cdot}3\ \mathrm{m.s}^{-1}$. Figure 15(a) pertains to translational displacements Y at 1000 rpm (sliding at $14.6\ \mathrm{m.s}^{-1}$), which results in rocking rotations ϕ with rotation vector parallel to the sliding direction. Figures 14(b) and 15(b) were simulated with our four-d.o.f. model. With proper choice of model parameters, particularly $\bar{y}$, μ, and T, agreement between experiment and simulation is good. The values of parameters used in Figures 14 and 15 "tuned" the model to the apparatus of reference [13]. Note that in going from Figures 14 to Figures 15, the rotational speed, and hence the sliding speed doubles. For the simulations to agree, the period T of the simulation's oscillations must be halved, as Figures 14(b) and 15(b) show.

This model can be used as a tool to design and understand how the slider interacts with the surface waviness to produce vibrations of a certain type. Characterization of surface topography, including surface waviness, generally requires many parameters. Thus surface waviness induced vibrations would also appear to require many parameters. The results of our study suggest that the equivalent contact point, with an appropriately chosen path type, can simplify these analyses. For the surface waviness present on the counter surface of reference [13], Figures 14 and 15 suggest that a *Type II* (straight line angled) path with parameter $\bar{y} = 0{\cdot}8\bar{x}$ is an acceptable model.

6. SUMMARY AND CONCLUSIONS

We simulated vibrations of a four-d.o.f. rigid-body sliding against smooth and wavy surfaces, and under special conditions analytically and numerically verified results of

Swayze and Akay [14]. Equations were highly non-linear. Stability analyses show that higher values of the torsional stiffnesses (Ω_ϕ, Ω_θ, and Ω_ψ) improve stability, while higher values of the static force $\bar{F}_{st}$ reduce stability by shrinking the domain of attraction around the origin. Excessive $\bar{F}_{st}$ could drive the system unstable. The system appears to be stable if the coefficient of friction μ is less than a critical value $\mu_{cr} = \alpha = h_x/h_z$, related to a ratio of slider dimensions.

Simulations for rigid bodies sliding against wavy countersurfaces employed an equivalent contact point that swept over selected paths on the slider's contact face. Four path types considered—*Type I* straight line back, *Type II* straight line angled, *Type III* sinusoid, and *Type IV* half-ellipse—displayed motions dependent on the path type. Traces generated by *Type I* and *Type IV* were similar, as were *Type II* and *Type III*. Natural frequencies significantly influenced responses.

Finally, the model was used to simulate experimental results [13] wherein the vibratory motions of a slider were constrained to four d.o.f. The simulation and experimental results were very similar, given appropriate choice of parameters in the model. The model could then be used as a mathematical tool to design proper patterns of surface waviness to generate beneficial vibrations that can control wear.

ACKNOWLEDGMENTS

The authors would like to thank the National Science Foundation, Grant CMS-9713942, Tribology program, Jorn Larsen-Basse program official, for support for this work.

REFERENCES

1. D. Godfrey 1967 *ASLE Transactions* **10**, 183–192. Vibration reduces metal to metal contact and causes an apparent reduction in friction.
2. V. Aronov, A. F. D'souza, S. Kalpakjian and I. Shareef 1984 *ASME Journal of Tribology* **106**, 54–58. Interactions among friction, wear, and system stiffness—Part 1: effect of normal load and system stiffness.
3. V. Aronov, A. F. D'souza, S. Kalpakjian and I. Shareef 1984 *ASME Journal of Tribology* **106**, 59–64. Interactions among friction, wear, and system stiffness—Part 2: vibrations induced by dry friction.
4. V. Aronov, A. F. D'souza, S. Kalpakjian and I. Shareef 1984 *ASME Journal of Tribology* **106**, 65–69. Interactions among friction, wear, and system stiffness—Part 3: wear model.
5. D. H. Hess and A. Soom 1991 *Journal of Tribology* **113**, 80–86. Normal vibrations and friction under harmonic loads: Part I—Hertzian contacts.
6. M. D. Bryant, A. Tewari and J. W. Lin 1995 *IEEE Transactions on Components, Hybrids & Manufacturing Technology* **18**, 375–381. Wear rate reductions in carbon brushes conducting current and sliding Against wavy copper surfaces
7. M. D. Bryant, D. York, and A. Tewari 1998 *Journal of Wear* **216**, 60–69. Effects of micro (rocking) vibrations and surface waviness on wear and wear debris.
8. A. U. Tewari 1994 *Master's Thesis, The University of Texas at Austin.* The effects of speed on wear particles and currents on wear rates in carbon brushes sliding against wavy and smooth copper surfaces.
9. M. D. Bryant and J. W. Lin 1993 *Journal of Wear* **170**, 267–279. Photoelastic visualization of contact phenomena between real tribological surfaces, with and without sliding.
10. J. W. Lin and M. D. Bryant 1996 *ASME Journal of Tribology* **118**, 116–124. Reductions in wear rate of carbon samples sliding against wavy copper surfaces.
11. J. W. Lin 1993 *PhD Dissertation, The University of Texas at Austin.* Visualization of the contact interface and observation of interface phenomena in sliding wear of carbon brushes.
12. D. G. York 1995 *Master's Thesis, The University of Texas at Austin.* The effects of vibrations on wear rates in carbon brushes sliding against smooth and wavy surfaces.

13. M. D. BRYANT and D. YORK 2000 *ASME Journal of Tribology* **122**, 374–380. Measurements and correlations of slider vibrations and wear.
14. J. L. SWAYZE and A. AKAY 1994 *Journal of Sound and Vibration* **173**, 599–609. Effects of system dynamics on friction-induced oscillations.
15. D. T. GREENWOOD 1988 *Principles of Dynamics*. Englewood Cliffs, NJ: Prentice-Hall, Inc.
16. L. F. SHAMPINE and M. W. REICHELT 1994 *Technical Report* 94-6, *Mathematical Department, Southern Methodist University, Dallas, TX*. The MATLAB ODE Suite.
17. L. F. SHAMPINE and M. K. GORDON 1975 *Computer Solution of Ordinary Differential Equations, The Initial Value Problem*. San Francisco: W. H. Freeman and Company.
18. C. PHOLSIRI 1997 *Master's Thesis, The University of Texas at Austin*. Vibrations of a four-degree-of-freedom rigid body sliding against a wavy surface.

APPENDIX A: EULER'S ANGLES

The transformation matrices can be obtained by observing Figure 16 along with the definitions of ψ, θ, and ϕ. The following equations describe the transformations.

$$\begin{Bmatrix} x' \\ y' \\ z' \end{Bmatrix} = \begin{bmatrix} \cos\psi & \sin\psi & 0 \\ -\sin\psi & \cos\psi & 0 \\ 0 & 0 & 1 \end{bmatrix} \begin{Bmatrix} X \\ Y \\ Z \end{Bmatrix}, \tag{A1}$$

$$\begin{Bmatrix} x'' \\ y'' \\ z'' \end{Bmatrix} = \begin{bmatrix} \cos\theta & 0 & -\sin\theta \\ 0 & 1 & 0 \\ \sin\theta & 0 & \cos\theta \end{bmatrix} \begin{Bmatrix} x' \\ y' \\ z' \end{Bmatrix}, \tag{A2}$$

$$\begin{Bmatrix} x \\ y \\ z \end{Bmatrix} = \begin{bmatrix} 1 & 0 & 0 \\ 0 & \cos\phi & \sin\phi \\ 1 & -\sin\phi & \cos\phi \end{bmatrix} \begin{Bmatrix} x'' \\ y'' \\ z'' \end{Bmatrix}. \tag{A3}$$

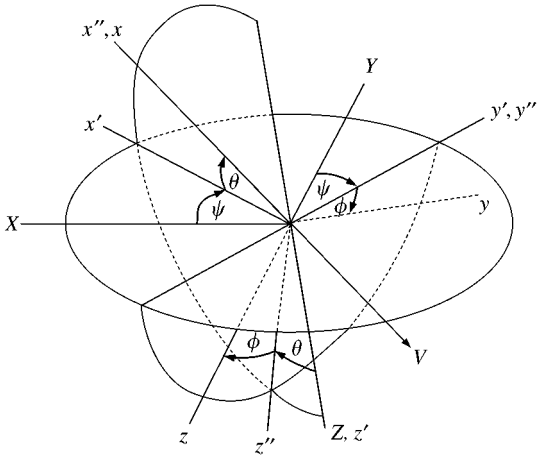

Figure 16. The Euler's angles.

Rewriting the above equations in shorter form, we obtain

$$\{v'\} = [T_\psi]\{V\}, \quad \{v''\} = [T_\theta]\{v'\}, \quad \{v\} = [T_\phi]\{v''\}$$

or

$$\{v\} = [T_\phi][T_\theta][T_\psi]\{V\} = [T]\{V\},$$

where $\{V\}$ is an arbitrary vector $\mathbf{v}$ in the fixed XYZ axes and $\{v\}$ represents the same vector in the rotating xyz co-ordinate system. The transformation matrix can be obtained by performing the matrix multiplications in the preceding equation.

$$\begin{Bmatrix} x \\ y \\ z \end{Bmatrix} = \begin{bmatrix} \cos\psi\cos\theta & \sin\psi\cos\theta & -\sin\theta \\ (-\sin\psi\cos\phi & (\cos\psi\cos\phi + & \\ +\cos\psi\sin\theta\sin\phi) & +\sin\psi\sin\theta\sin\phi) & \cos\theta\sin\phi \\ (\sin\psi\sin\phi & (-\cos\psi\sin\phi + & \\ +\cos\psi\sin\theta\cos\phi) & \sin\psi\sin\theta\cos\phi) & \cos\theta\cos\phi \end{bmatrix} \begin{Bmatrix} X \\ Y \\ Z \end{Bmatrix}, \tag{A4}$$

Because of the orthogonality of the transformation matrix, inverse transformations may be obtained by simply transposing $[T]$.

$$\{V\} = [T]^{\mathrm{T}}\{v\}. \tag{A5}$$

Note that this transformation matrix assumes a sequence of rotations: ψ, θ, and then ϕ. If the sequence differs from this, it would result in a different transformation matrix. However, the assumption that angular displacements are small makes the order in the sequence insignificant.

APPENDIX B: NOMENCLATURE

$b_z, b_\phi, b_\theta, b_\psi$	damping coefficients about axes
h_x, h_y, h_z	dimensions of rigid body
I_{xx}, I_{yy}, I_{zz}	rotational inertias of rigid body about x
F_n	normal force
F_μ	friction force
F_{st}	static load on slider
F_{wav}	normal force due to surface waviness
$k_z, k_\phi, k_\theta, k_\psi$	stiffnesses about axes
m	mass of rigid sliding body
t	time
V	potential energy
U	sliding speed, see Figure 1
$(X, Y, Z), (x, y, z)$	inertial and attached co-ordinates, see Figure 1
ϕ, θ, ψ	Euler angles for rotations about (x, y, z)
μ	friction coefficient
μ_{cr}	critical friction coefficient for stability
$\omega'_x, \omega'_y, \omega'_z$	rotational speeds about (x, y, z)
$\omega_z, \omega_\phi, \omega_\theta, \omega_\psi$	natural frequencies, section 3

Non-dimensional variables (*section* 3)

$\bar{F}_n, \bar{F}_{st}, \bar{F}_{wav}$	non-dimensional forces
$\bar{x}, \bar{y}$	non-dimensional path co-ordinates

$c_x, c_y, c_z, d_x, d_y, d_z$	non-dimensional groups, see equations (13)
$a_\phi, a_\theta, \bar{F}_n$	non-dimensional groups, see equations (13)
α, β	length ratios, section 3
γ, λ, η	inertia ratios
τ	dimensionless time
$\Omega_\phi, \Omega_\theta, \Omega_\psi$	frequency ratios
$\zeta_z, \zeta_\phi, \zeta_\theta, \zeta_\psi$	damping ratios

Notations and subscripts

$(\,)'$	$\equiv \mathrm{d}/\mathrm{d}\tau$
$(\dot{\cdot})$	$\equiv \mathrm{d}/\mathrm{d}t$
$\bar{F}$	non-dimensional variable F, section 3
e	equilibrium points